

# Unsupervised cell identification on multidimensional X-ray fluorescence datasets

Siwei Wang,<sup>a,\*</sup> Jesse Ward,<sup>b</sup> Sven Leyffer,<sup>a</sup> Stefan M. Wild,<sup>a</sup> Chris Jacobsen<sup>b,c,d</sup> and Stefan Vogt<sup>b</sup>

<sup>a</sup>Mathematics and Computer Science Division, Argonne National Laboratory, 9700 South Cass Avenue, Argonne, IL 60439, USA, <sup>b</sup>Advanced Photon Source, Argonne National Laboratory, 9700 South Cass Avenue, Argonne, IL 60439, USA, <sup>c</sup>Department of Physics and Astronomy, Northwestern University, 2145 Sheridan Road, Evanston, IL 60208, USA, and <sup>d</sup>Chemistry of Life Processes Institute, Northwestern University, 2170 Campus Drive, Evanston, IL 60208, USA.  
\*E-mail: siweiw@gmail.com

A novel approach to locate, identify and refine positions and whole areas of cell structures based on elemental contents measured by X-ray fluorescence microscopy is introduced. It is shown that, by initializing with only a handful of prototypical cell regions, this approach can obtain consistent identification of whole cells, even when cells are overlapping, without training by explicit annotation. It is robust both to different measurements on the same sample and to different initializations. This effort provides a versatile framework to identify targeted cellular structures from datasets too complex for manual analysis, like most X-ray fluorescence microscopy data. Possible future extensions are also discussed.

**Keywords:** X-ray fluorescence microscopy (XFM); unsupervised object recognition; cell identification; trace element distributions; modeling overlapping cells.

© 2014 International Union of Crystallography

## 1. Introduction

X-ray fluorescence microscopy (XFM) provides submicrometer-resolution information on the localization and quantity of all but the lightest elements. For studies of micrometer-thick biological specimens, it provides this information with lowest dose for a given elemental sensitivity (Kirz, 1980), so that it has emerged as a powerful method for studies in biology and medicine (Paunesku *et al.*, 2006). By using high-resolution optics such as Fresnel zone plates, multi-keV X-rays are focused to a small spot through which the specimen is scanned. Absorption of these X-rays leads to the ejection of core shell electrons, and photons at characteristic elemental fluorescence energies are emitted as outer-shell electrons fill the core shell vacancies. A competing process of emission of Auger electrons reduces the fluorescence yield (*i.e.* the efficiency of conversion of electron holes to characteristic X-ray fluorescence, in particular for the lighter elements). Even then, X-ray fluorescence detection is still the preferred mode of contrast for elemental mapping because the escape depth of Auger electrons from the sample is extremely limited (Tan *et al.*, 1982).

An energy-dispersive detector is used to record the energy of individual X-ray fluorescence photons, thus providing information on elemental content at that pixel location. These multispectral data typically contain 1000 or more energy channels per pixel, which in our case have been analyzed to obtain concentrations of chemical elements as described in §3.

We are not the first to recognize that scientific capability for intuitive understanding is being overwhelmed by the volume and complexity of data generated in modern microscopies. In light microscopy, Swedlow *et al.* (2009) have noted that ‘multidimensional imaging has driven a revolution in modern biology, yet the significant data management and analysis challenges presented by these new complex datasets remain largely unsolved’. In recognition of these challenges, we have already made some progress. Members of our team have written a program called *MAPS* (Vogt, 2003) for quantification and fitting of multidimensional X-ray fluorescence images and a cluster-analysis-based program *PCA\_GUI* for classification and analysis in soft X-ray spectromicroscopy (Lerotic *et al.*, 2004, 2005) (this program has migrated to an open-source project at <http://code.google.com/p/spectromicroscopy>). *MAPS* carries out the analysis required to go from per-pixel fluorescence spectra to per-pixel elemental concentration, along with analysis through the manual generation of spatial regions of interest; enhancements to include principal component analysis and clustering are promising but not yet reliable enough for unsupervised analysis of large datasets. *PCA\_GUI* provides cluster analysis but suffers from negative unphysical weightings in some analyses (now being addressed through the use of non-negative matrix factorization). Other software packages have also been developed to analyze X-ray fluorescence datasets, for example *PyMCA* (Solé *et al.*, 2007) as well as *GeoPIXE* (Ryan *et al.*, 2002). Each of these

packages tends to have specific areas they are optimized for; but, overall, these efforts do not yet appear to be as advanced as clustering and machine-learning analysis implemented in optical microscopy (Ljosa & Carpenter, 2009) or hyperspectral analysis used in aircraft and satellite imaging (Plaza *et al.*, 2004). Our goal here is to provide object recognition directly from X-ray fluorescence spectra with no subsequent higher-level processing required, so as to greatly enhance how we approach and understand the rich data sets generated from X-ray fluorescence excitation in electron, proton and X-ray excitation microscopy methods.

Based on optical microscopy, magnetic resonance imaging and other medical imaging modalities, many object recognition methods are proposed to automatically (Wolz *et al.*, 2010; Arteta *et al.*, 2012; Cortés & Amit, 2008) or semi-automatically (Aydin *et al.*, 2010; McCullough *et al.*, 2008; Lin *et al.*, 2003) identify cellular structures. However, cell identification using XFM has unique challenges. Firstly, it requires modeling a large number of chemical elements simultaneously. Most of the methods focused on optical microscopy can only deal with one or several independent intensity channels. Secondly, there is no known manual annotation dataset to serve as a large-scale training example, hence most supervised learning approaches [support vector machines (Kasson *et al.*, 2005; Tao *et al.*, 2007; Wang *et al.*, 2007), Markovian random fields, min-max flow graph cut (Wolz *et al.*, 2010; Yin *et al.*, 2010), Potts model (Russell *et al.*, 2007)] are not applicable. Thirdly, modeling overlapping cellular structures in XFM datasets is more challenging compared with that in other related imaging problems; an XFM dataset provides pixel-level localization and quantity of elements. Therefore, it is necessary to model how different cells overlap with each other. Nevertheless, most known methods do not model cell overlap explicitly; instead they either generate nonoverlapping regions from overlapping cells (Arteta *et al.*, 2012; Lin *et al.*, 2003) or only process cells at most touching at their boundaries (Bergeest & Rohr, 2011, 2012). In §7, we will discuss the difference between our method and a representative cell counting routine ('analyze particle' from *ImageJ*) in more detail.

We propose here a novel unsupervised cell identification approach to tackle these unique challenges of XFM datasets. Without manual annotations, our approach can locate, identify and refine positions and areas of cellular structures (including overlapping cells) based on their elemental content from a large number of elements simultaneously.

To demonstrate this approach, we apply it to a dataset of three intermixed cell types. We begin by using *MAPS* to reduce the acquired fluorescence spectra into quantitative concentrations of nine chemical elements. As input parameters for subsequent analysis, the approach accepts lower bounds of cell sizes, averages and standard deviations of cell contents from a few hand-drawn regions of interest (ROIs) for each type. (These hand-drawn ROIs can in the future be replaced by representative contents from other reference data or learned automatically.) Then we use a generalized likelihood ratio test to model the configuration of multiple overlapping cells. Afterward, we apply two procedures [boundary

delineation (§4.3) and pixel refinement (§4.4)] to further improve the boundaries of identified cells.

The paper is organized as follows. In §2, we provide a high-level description of the components of our problem and approach. In §3, we discuss sample preparation, data acquisition and the datasets we employed in evaluating the consistency and robustness of this approach. We will also provide specific assumptions for our test dataset with respect to our general assumptions in §2. In §4, we introduce the four underlying procedures in detail: preprocessing, estimating group configuration, boundary delineation and pixel refinement. Currently, each procedure can be viewed as solving an optimization problem, the solution of which is then passed as an input to the next procedure. However, this approach can be modified such that the output of the last step can serve as the input to the first step. We report our results in §5 and demonstrate that this approach generates robust statistics of cell populations with respect to initial parameters in §6. Since this cell identification approach is in early stages of development, many opportunities for improvement remain, and we will discuss some of them in §7.

## 2. Problem and overview

We address the fundamental question: 'Where are the (whole) cells?' based on recorded elemental content in an XFM dataset. The goal of our approach is to identify cells of different types, while also allowing for multiple cells to overlap. We give a broad overview of our approach here, which is described in detail in §4.

A key difficulty here is that often no manual annotation is available to serve as a reference; we only know both the total elemental contents of the whole cell areas and shape, and size of cells of a given type can be employed as salient features. We use the following two classes of expert-informed cell features to initialize this approach:

(i) *Morphology*. We assume that all cells of a specific type have somewhat similar sizes and shapes.

(ii) *Content*. We assume that cells of a specific type have similar total content in their characteristic elements, and that these characteristic elemental contents are distinct compared with cells of other types.

The initial inputs for this approach are thus information on the morphology and content features. Preprocessing of the putative cells (§4.1) is done by image segmentation.

We first divide pixels of the image of a given characteristic element into foreground and background components (*i.e.* based on their intensity). We then partition all foreground pixels into groups *via* the recursive min-cut algorithm (Dhillon *et al.*, 2007) and then fit a minimum-area ellipse around each of these segments as the initial guess of cell areas. Here, we deliberately initialize the partitioning algorithm so that we oversegment (*i.e.* all actual cells are covered with at least one group). We chose this algorithm because it is unsupervised and oversegmentation is straightforward.

This oversegmentation conditions the configuration estimation procedure in §4.2 to focus on evaluating group

configurations with potentially reduced number of cell groups. This estimation procedure determines whether merging two groups or deleting a group will represent the total content better than the current configuration. We represent the total content criteria with Gaussian distributions (specified by a mean and diagonal covariance) obtained from the given content inputs.

After we estimate the configuration of cell groups, we refine these putative cell groups by adjusting their boundaries based on a total elemental content criteria (see §4.3). This procedure aims at recovering pixels that are within a cell but were initially relegated to the background because of thresholding. For every boundary we obtain by this procedure, we compensate for potential smoothness discrepancies using a pixel refinement procedure (see §4.4). This procedure ensures that the resulting areas cover the group of pixels best for their corresponding cells.

This multistep approach is versatile and can be applied to a broad class of identification problems. The components described here can also be employed independently or combined to answer different scientific questions. An overview of this approach is presented in Procedure 1. Table 1 in the supporting information illustrates all steps of this procedure.<sup>1</sup>

**Procedure 1.** Overview of the approach.

**Inputs:** pixels  $P$  of an XFM dataset, cell types  $\mathcal{T}$ , characteristic element  $e_t$  and lower bound of size  $s_t$  for all  $t \in \mathcal{T}$ , means and standard deviations of representative cell contents;

- Preprocessing;

**for all**  $t \in \mathcal{T}$

Obtain foreground and background of  $e_t$ ;

Partition foreground pixels using elemental map of  $e_t$ , such that all segments contain at most  $s_t$  pixels;

Obtain groups  $\mathcal{G}_t$  of type  $t$  by using minimum-area ellipses to cover all individual segments;

**end for**

- Estimation of group configuration: obtain groups  $\hat{\mathcal{G}}$  from initial groups  $\mathcal{G} = \cup_t \mathcal{G}_t$  by either merge or deletion;

- Optimization of group boundaries: delineate boundaries of all groups  $g \in \hat{\mathcal{G}}$  using both morphology and content features;

- Local pixel refinement: refine pixel boundaries of all  $g \in \hat{\mathcal{G}}$ .

### 3. Sample and data

We deliberately chose a combination of very different cell types to verify that the algorithm is able to work with this diversity, and to make sure a human observer can easily test the accuracy of the algorithm (differentiation between two very similar subpopulations can be achieved by statistically analyzing extracted elemental content resulting from our algorithm). The specific cell types were chosen on the basis of

availability, use as model systems elsewhere in biology, and expected differences in elemental content, cell size and morphology. Red blood cells have a well known dumbbell shape, and were expected to contain relatively more iron than other cell types because of the presence of heme iron in hemoglobin (Hawkins *et al.*, 1954), and little else. By comparison, yeast cells are expected to be smaller, and have high Zn as well as P content (Marvin *et al.*, 2012). As a third cell type with a complementary elemental content we chose the green algae *Chlamydomonas* with high manganese levels because of the presence of manganese in photosystem II (Dismukes, 1986).

Washed and pooled rabbit red blood cells (rbc) at 10% hematocrit were purchased from Lampire Biological Laboratories (Pipersville, PA, USA). A 1 ml volume sample was drawn and centrifuged for 10 min at 600g. The supernatant was discarded, and cells were resuspended in a solution of 200 mM sucrose and 10 mM PIPES (Good *et al.*, 1966), both from Sigma-Aldrich (St Louis, MO, USA). Yeast cells were inoculated in 2.5 ml of sterile YPD media (Lundblad & Struhl, 2001) and grown in a shaking incubator at 303 K and 300 r.p.m. for 24 h. A 1 ml volume sample was drawn and centrifuged for 10 min at 600g. The supernatant was discarded, and cells were resuspended in a solution of 200 mM sucrose and 10 mM PIPES.

Algae cells were provided by Qiaoling Jin (Argonne). The wild-type strain of *Chlamydomonas reinhardtii* was purchased from ATCC (Manassas, VA, USA) and grown mixotrophically in TAP medium (Gorman & Levine, 1965) on a rotary shaker (120 r.p.m.) at 298 K and in the presence of  $\sim 100 \mu\text{mol photons m}^{-2} \text{ s}^{-1}$  of photosynthetically active light. A 1 ml volume sample was drawn and centrifuged for 2 min at 600g. The supernatant was discarded, and cells were resuspended in a solution of 200 mM sucrose and 10 mM PIPES. Equal volumes of red blood cells, yeast cells and algae cells were suspended in 200 mM sucrose and 10 mM PIPES and then mixed together. A 2  $\mu\text{L}$  volume was spotted onto a 200 nm-thick silicon nitride window (Silson Ltd, Northampton, UK) and allowed to air dry overnight.

X-ray fluorescence imaging was performed at beamline 2-ID-E at the Advanced Photon Source at Argonne, USA. Undulator-produced X-rays at 10 keV incident energy were focused to a spot size of 0.8  $\mu\text{m}$  by 0.8  $\mu\text{m}$  using Fresnel zone plate optics (Xradia Inc., Pleasanton, CA, USA). Samples were raster-scanned through the X-ray beam in fly-scanning mode, covering about a  $(200 \mu\text{m})^2$  area with a pixel size  $\delta = 0.3 \mu\text{m}$  in each direction,  $666 \times 667$  pixels, and an effective dwell time of 100 ms per pixel. Full fluorescence spectra were detected at each pixel using a four-segment silicon drift detector (Vortex-ME4, Hitachi High-Technologies Science America, Northridge, CA, USA), with each detector segment collecting a slightly different signal because of angular variations in scattered signals, different self-absorption paths to the segment, and so on. These differences, resulting from the 15° angle between the sample and the detector, are negligible for high- $Z$  elements, but can be significant for low- $Z$  elements (e.g. 50% for P).

<sup>1</sup> Supporting information for this paper is available from the IUCr electronic archives (Reference: WA5055).

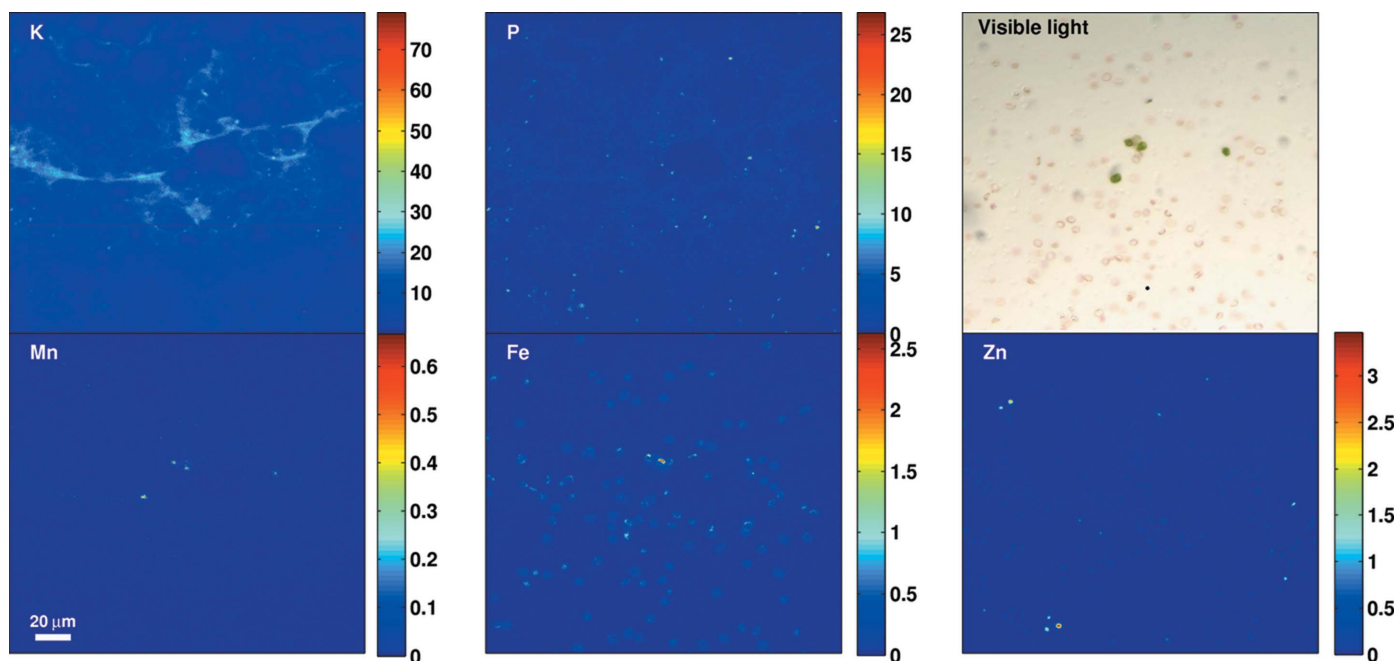


**Figure 1**

Elemental maps for K, P, Mn, Fe and Zn, and visible-light micrograph of a mixture of three cell types (red blood cells, algae, yeast) used for subsequent analysis. The quantified elemental content per pixel is shown in  $\mu\text{g}/\text{cm}^2$  in the intensity scale next to each map. The maps of particular elements obtained by X-ray fluorescence microscopy hint at the characteristics of the different cell types: Mn is prevalent in algae and Fe in red blood cells, while Zn and P are indicative of yeast cells. The visible-light micrograph was acquired at one focal plane and thus does not show all cells; slight distortions in relative cell positions between the X-ray fluorescence maps and the visible-light micrograph are due to differences in viewing angles.

Every pixel in the XFM dataset originally contains the full X-ray spectra recorded from the four detector segments. These spectra were then processed by *MAPS* (Vogt, 2003), which involves a fitting procedure and calibration based on a standard with known elemental concentration to yield quantitative maps of elemental concentration in  $\mu\text{g}/\text{cm}^2$ . Those quantitative maps for the elements P, S, Cl, K, Ca, Mn, Fe and Zn provided the input data for the analysis procedures described here (Fig. 1).

Based on this specific information, we can derive the following features for identifying cells in this test dataset:

(i) Morphology: all cells can be modeled as ellipses with different sizes and shapes.

(ii) Content: all cells have consistent content in all nine elements (P, S, Cl, K, Ca, Mn, Fe, Cu, Zn) resembling Gaussian distributions. For each cell type, there is a characteristic element which provides signature elemental content information, *i.e.* Fe for red blood cells, Zn for yeast cells and Mn for algae cells.

#### 4. Detailed description of our approach

Here, we describe four individual components of Procedure 1 in detail. For a given image, we let  $P$  denote the set of pixels in the image, with each pixel indexed by a pair of (column, row) indices  $(x, y)$ . We use uppercase roman letters to denote sets of pixels and use calligraphic letters to refer to other types of sets (*e.g.* index sets, elements, cell types) throughout the sequel.

Let  $F$  and  $B$  denote disjoint sets of foreground and background pixels, respectively, so that  $P = F \cup B$ . We designate a *group of pixels* by  $G_g$ , where  $g \in \mathcal{G}$  denotes a group index. Each group will have an associated type  $t \in \mathcal{T}$ ; in this paper  $\mathcal{T} = \{\text{algae, rbc, yeast}\}$ . Groups will ultimately be used to define a cell, but we use the term ‘group’ to acknowledge that, particularly in the initial steps of this approach, there may not be a one-to-one correspondence between groups and cells. The collection of all groups defines the foreground pixels as  $F = \bigcup_{g \in \mathcal{G}} G_g$ . Associated with each group  $G_g$  will be a set of local background pixels  $B_g$ , more formally defined in §4.1.2.

A *region*  $R_r$  (with  $r \in \mathcal{R}$ ) consists of pixels belonging to one or more groups and their local backgrounds. We let  $\mathcal{G}_r \subseteq \mathcal{G}$  denote the set of groups belonging to region  $R_r$ , so that  $R_r = \bigcup_{g \in \mathcal{G}_r} (G_g \cup B_g)$ . The sets  $\mathcal{G}_r$  form a partitioning of  $\mathcal{G}$ . We denote the local background of region  $R_r$  by  $B_r$  (defined in §4.1.2).

In this paper, we limit the content computation to  $|\mathcal{E}| = 9$  elements,  $\mathcal{E} = \{\text{P, S, K, Cl, Ca, Mn, Fe, Cu, Zn}\}$ . For a general set of pixels  $Z$ , we define  $c_e(Z)$  to be the total content of  $Z$  in  $e$  by summing over all pixels in  $Z$  using the elemental map for element  $e \in \mathcal{E}$ . For example, for a single pixel  $Z = (x, y)$ , we use  $c_e(x, y)$  to denote the content using the *content map* for element  $e \in \mathcal{E}$  (see §3).

Using these notations, we organize our approach as follows:

(i) *Preprocessing and image segmentation.* Specify elemental contents for each cell type, identify the foreground pixels  $F$ , divide the foreground into  $|\mathcal{G}|$  possibly overlapping groups, and aggregate the groups into  $|\mathcal{R}|$  disjoint regions (§4.1). The putative groups serve as an initialization; they may

be deleted or merged to other groups in subsequent cell identification procedures (see Fig. 4).

(ii) *Estimation of group configuration.* Given a set of groups  $\mathcal{G}$  and a set of disjoint regions  $\mathcal{R}$ , adjust the number and areas of groups of each type within each region to best match the observed elemental contents (§4.2).

(iii) *Optimization of group boundaries.* Given putative cell groups in each region, determine smooth curves to serve as boundaries of the cells (§4.3).

(iv) *Local pixel refinement.* For the smooth boundaries in a region that do not satisfy local optimality conditions, refine each associated group so the content of its discrete set of pixels best matches the content in a cell (§4.4).

To seed our preprocess procedure, we use per-hand identification of ROIs around a few isolated cells of each type. This was appropriate for an initial study, though in the future the seeding could be done from literature values for elemental composition and area  $s_t$ .

In our case, the ROIs provide twofold information: (i) the element or combination of elements provides characteristic elemental maps that distinguish each specified cell type, and (ii) the content from these ROIs is employed as representative total elemental content of these cells. We use the former information to preprocess the dataset and obtain initial guesses for the areas of putative cells (§4.1.1). We use the latter to refine these putative cells (§4.1.4).

#### 4.1. Preprocessing and image segmentation

The first procedure is responsible for producing the representative elemental distributions, a set of initial groups  $\mathcal{G}$  and regions  $\mathcal{R}$ , and the local backgrounds for each of these groups and regions.

**4.1.1. Initial group formation.** The input of the image segmentation algorithm are the individual elemental maps based on hand-drawn ROIs and the segment area bound  $s_i$ ; for purposes of oversegmentation,  $s_i$  is taken to be the smallest cell area from the hand-selected ROI. The three cell types have somewhat different sizes. We therefore set the  $s_t$  value of each type  $t \in \mathcal{T}$  for subsequent analysis: we used  $s_t = 200$  pixels (or  $18 \mu\text{m}^2$ ) for red blood and algae cells, and  $s_t = 30$  pixels (or  $2.7 \mu\text{m}^2$ ) for yeast cells.

Using the individual elemental maps and segment area bound  $s_t$  for all types in  $\mathcal{T}$ , we then perform an image segmentation using images from three characteristic elements (Mn for algae, Fe for red blood cells and Zn for yeast). The resulting segments (shown in Fig. 2) each locate a possible area for a cell of type  $t$ .

Based on these segmentations, we form minimum-area ellipses to cover pixels belonging to the same segment. Ellipses are appropriate for the cell types considered here; more complicated shapes can also be considered. The pixels in each ellipse are used to define an initial group  $G_g$ . By construction, all groups contain a contiguous set of pixels.

**4.1.2. Region formation and background content.** As previously described, a region is defined as an area of groups and their local backgrounds. Here, the local background  $B_g$  of

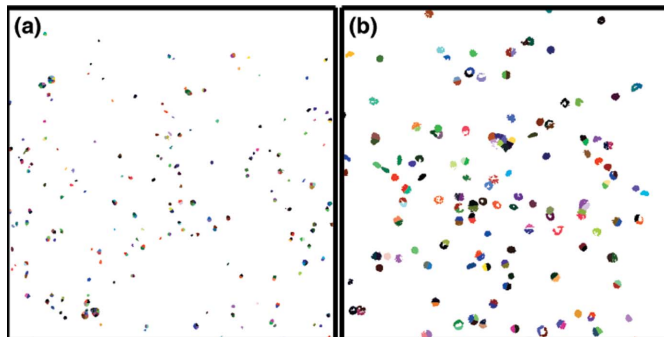


**Figure 2**

Image segmentation result used to form the initial groups for yeast and red blood cells based on the markers Zn (a) and Fe (b), respectively. Algae cells are not shown because there are only five cells. All pixels of the same color belong to the same segment, hence they are treated as one single putative cell group in subsequent procedures.

a group  $G_g$  is defined as a set of pixels within a distance  $\Delta > 0$  of the group,

$$B_g \equiv \{(x, y) \in B : |x - \hat{x}| + |y - \hat{y}| \leq \Delta \text{ for some } (\hat{x}, \hat{y}) \in G_g\}, \quad (1)$$

where we recall that the foreground is defined as  $F = \cup_{g \in \mathcal{G}} G_g$  and the background is defined as  $B = P \setminus F$ .

Therefore, a region  $R_r = \cup_{g \in \mathcal{G}_r} (G_g \cup B_g)$  contains groups that are either overlapping with each other or overlapping in their local backgrounds. The local background of a region is then defined in analogy to equation (1) as the background outside of the region that is within a distance  $\Delta$  of the region, or

$$B_r \equiv \{(x, y) \in B \setminus R_r : |x - \hat{x}| + |y - \hat{y}| \leq \Delta \text{ for some } (\hat{x}, \hat{y}) \in R_r\}. \quad (2)$$

Although groups (as well as their backgrounds) may overlap, the regions are disjoint. Thus a region provides a convenient partitioning of the image into semi-independent structures, while groups allow for the modeling of overlapping cells. Initial groups, regions and local backgrounds for the entire test dataset are illustrated in Fig. 3.

The primary purpose of obtaining local backgrounds is to adaptively estimate the local background content. Knowledge of the background content is important in XFM analysis. When using energy-dispersive detectors to record the fluorescence signal, there will be some contribution at all energies as a result of inelastic scattering and incomplete collection of the charge deposited in the detector by fluorescence photons (ideally this is resolved by the fitting procedure of *MAPS* as described in §3). There may also be some signal as a result of elements in the medium in which the cells were prepared. The inhomogeneous background (see, for example, the K channel in Fig. 1) in many of the elemental maps introduces challenges for cell identification and for generating statistics on elemental content of various cell types.

Analogous to total cell content introduced in §2, we also use Gaussians to describe per-pixel local background content. For

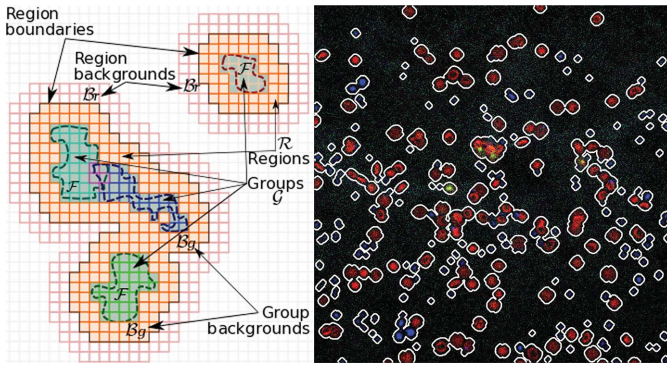


**Figure 3**  
 (a) Illustration of groups (foreground pixels), regions and backgrounds with corresponding mathematical notations. The innermost solid boundaries represent the union of groups, the next boundaries (black, orange fill) represent the regions, and the outermost boundaries (pink) represent the union of regions and region backgrounds. (b) Overlay showing distributions of Fe (red), Mn (green), Zn (blue) and the region boundaries (white). Note that (a) illustrates a  $\Delta = 2$  pixel distance; we use a  $\Delta = 5$  pixel distance for both group and region background estimation in our experiments.

example,  $\mu_{er}$  denotes the mean (per-pixel) content of element  $e$  in the local background of region  $R_r$ , and is defined as

$$\mu_{er} \equiv \frac{1}{|B_r|} c_e(B_r) = \frac{1}{|B_r|} \sum_{(x,y) \in B_r} c_e(x,y). \quad (3)$$

We similarly define the sample variance in the local background  $B_r$ ,

$$\sigma_{er}^2 \equiv \frac{1}{|B_r| - 1} \sum_{(x,y) \in B_r} \left[ c_e(x,y) - \frac{1}{|B_r|} c_e(B_r) \right]^2. \quad (4)$$

**4.1.3. Representative cell elemental content.** For the subsequent procedures we require statistics of the content of each type of cell to broadly characterize the types of cells.

In the current approach, we represent the distribution of the total elemental content in a cell as a truncated (imposing non-negativity) Gaussian. Although other distributions can be used in our framework, we focus on Gaussians here to illustrate the method based on a small number of distributional parameters. In particular, if we assume that the contents for cells of different types and elements are independent, we need only to specify means and variances ( $\mu_{et}, \sigma_{et}^2$ ) for all  $e \in \mathcal{E}$  and  $t \in \mathcal{T}$ .

If such information is unavailable, it can be estimated by using a small number of expert hand-selected cells, particularly those that are well separated from other cells in this particular example. Given a collection  $\mathcal{G}'(t)$  of hand-selected groups corresponding to cells of type  $t$ , we can use the sample mean

$$\hat{\mu}_{et} = \frac{1}{|\mathcal{G}'(t)|} \sum_{g \in \mathcal{G}'(t)} c_e(G_g) \quad (5)$$

and sample variance

$$\hat{\sigma}_{et}^2 = \frac{1}{|\mathcal{G}'(t)| - 1} \sum_{g \in \mathcal{G}'(t)} [c_e(G_g) - \hat{\mu}_{et}]^2 \quad (6)$$

as estimates for  $\mu_{et}$  and  $\sigma_{et}^2$ , respectively.

**4.1.4. Content computation for groups.** Here we describe how to compute content for groups. Because we allow groups to overlap, it is necessary to apportion the content given by an elemental map among overlapping groups. A naïve way to distribute the content  $c_e(x,y)$  would be to split it equally among the groups that contain the pixel  $(x,y)$ . The approach that we take is to account for the relative abundance of the element with respect to the group's type. Another way to describe this is to split pixel content between groups which contain that pixel weighted to the mean content per group and type. For this we employ the representative means  $\mu_{et}$  as estimated in §4.1.3.

Formally, we let  $\mathcal{G}_t(x,y) \subseteq \mathcal{G}$  denote the set of groups of type  $t \in \mathcal{T}$  that contain pixel  $(x,y)$ . A single group of type  $t$  containing  $(x,y)$  is thus assigned the fraction of content

$$f_{et}(x,y) = \frac{\mu_{et}}{\sum_{t' \in \mathcal{T}} |\mathcal{G}_{t'}(x,y)| \mu_{et'}}. \quad (7)$$

By construction, the content from an elemental map is preserved: summing over all groups containing  $(x,y)$  yields the elemental map content  $c_e(x,y)$ . Taking into account the background's contribution and using this weighting, we define the assigned content of element  $e \in \mathcal{E}$  for group  $g \in \mathcal{G}$  of type  $t \in \mathcal{T}$  by

$$c_{egt} = \sum_{(x,y) \in G_g} f_{et}(x,y) [c_e(x,y) - \mu_{er}], \quad (8)$$

where  $r \in \mathcal{R}$  denotes the region that group  $G_g$  belongs to.

## 4.2. Estimation of group configuration

The image segmentation in §4.1 is used to provide an initial group configuration (*i.e.* numbers and areas of groups). However, two drawbacks prevent this configuration from serving as putative cell areas: (i) only a single trace element for each cell type is taken into account, whereas cells are usually represented with multiple elements in XFM datasets; and (ii) overlapping cells of the same type are not taken into account.

We now introduce an iterative procedure for adjusting this initial group configuration to a more realistic configuration. In each iteration, the current configuration is updated to better match the region content with respect to the representative cell contents (from §4.1.3). We use a generalized likelihood ratio (GLR) test to determine whether such an update would improve the configuration for region  $R_r$ . This GLR test is formulated as (Wasserman, 2003)

$$\frac{\max_{\Theta_0} \mathcal{L}(H_0 | c_r)}{\max_{\Theta_0^C} \mathcal{L}(H' | c_r)}. \quad (9)$$

The null hypothesis parameter space  $\Theta_0 = \{H_0\}$  has the current group configuration as its only hypothesis; the complementary parameter space  $\Theta_0^C$  has alternative hypotheses with reduced

numbers of groups. We need only to consider alternative hypotheses with fewer groups  $|\mathcal{G}'| < |\mathcal{G}_r|$  (Wu & Nevatia, 2009) because of the oversegmentation discussed in §4.1.

Even if we only reduce the number of groups, testing all possible configurations is still prohibitive. To make this GLR test computationally tractable, we limit the parameter space  $\Theta_0^C$  to alternative hypotheses of exactly  $|\mathcal{G}_r| - 1$  groups, either through merging two groups  $g, g' \in \mathcal{G}_r$  (forming a new group from  $G_g \cup G_{g'}$ ) or deleting a group  $g \in \mathcal{G}_r$ .

The data here are the elemental content  $c_r = (c_{re})$  of all pixels in region  $R_r$ . Assuming the contents of groups in a region are independent, we can cast  $c_r$  as the sum of the contents  $[c_g = (c_{egt})]$  in the groups  $g \in \mathcal{G}_r$  and the contents  $[c_{br} = (c_{ebr})]$  in the respective local backgrounds  $\cup_{g \in \mathcal{G}_r} B_g$ . Formally, for all  $e \in \mathcal{E}$  we have

$$c_{re} = \sum_{(x,y) \in (G_g, g \in \mathcal{G}_r)} c_e(x, y) = c_{ebr} + \sum_{g \in \mathcal{G}_r} c_{egt}, \quad (10)$$

where  $c_{egt}$  is defined in equation (8). The likelihood of our null hypothesis is thus evaluated as

$$\mathcal{L}(H_0|c_r) = \left[ \prod_{g \in \mathcal{G}_r} \mathcal{L}(H_0|c_g) \right] \mathcal{L}(H_0|c_{br}). \quad (11)$$

The mean and variance of element  $e$  for group  $g$  (of type  $t$ ) in region  $R_r$  are defined by

$$\tilde{\mu}_{egr} = \mu_{er}|G_g| + \hat{\mu}_{et} \quad \text{and} \quad \tilde{\sigma}_{egr}^2 = \sigma_{er}^2|G_g| + \hat{\sigma}_{et}^2,$$

where  $\hat{\mu}_{et}$  and  $\hat{\sigma}_{et}^2$  are defined in equations (5) and (6). The likelihood  $\mathcal{L}$  of group  $g$  is

$$\mathcal{L}(H_0|c_g) = \left( \prod_{e \in \mathcal{E}} 2\pi\tilde{\sigma}_{egr}^2 \right)^{-1/2} \exp \left[ -\frac{1}{2} \sum_{e \in \mathcal{E}} \frac{(c_{egt} - \tilde{\mu}_{egr})^2}{\tilde{\sigma}_{egr}^2} \right]. \quad (12)$$

The likelihood of the background is defined similarly, with the background mean and variance of element  $e$  defined by

$$\tilde{\mu}_{ebr} = \mu_{er} \left| \bigcup_{g \in \mathcal{G}_r} B_g \right| \quad \text{and} \quad \tilde{\sigma}_{ebr}^2 = \sigma_{er}^2 \left| \bigcup_{g \in \mathcal{G}_r} B_g \right|.$$

The likelihood of an alternative hypothesis  $H'$  is evaluated similarly to the null hypothesis in equation (11). In the merging and deleting operations, we now need only to modify the appropriate terms corresponding to the configuration differences between  $H_0$  and  $H'$ :

(i) *Merging*. If  $H'$  corresponds to merging adjacent groups ( $g, g'$ ), by convention the resulting group inherits the type  $t$  from the first group  $g$  [we also consider the pair  $(g', g)$ ]. The new group has content computed by using the pixels  $G_g \cup G_{g'}$  in equation (8). The updated means and variances for the new group  $g''$  are given by

$$\tilde{\mu}_{eg''r} = \mu_{er}|G_{g'} \cup G_g| + \hat{\mu}_{et} \quad \text{and} \quad \tilde{\sigma}_{eg''r}^2 = \sigma_{er}^2|G_{g'} \cup G_g| + \hat{\sigma}_{et}^2.$$

(ii) *Deleting*. If  $H'$  corresponds to deleting group  $g$ , then we expand the background with all pixels only in group  $g$ . Those pixels are

$$G_g^* \equiv \{(x, y) \in G_g : \forall g' \in \mathcal{G}_r \setminus \{g\}, (x, y) \notin G_{g'}\}. \quad (13)$$

In the evaluation of joint likelihood, we drop the term with respect to  $c_g$  and update background means  $\tilde{\mu}_{eb'r}$  and variances  $\tilde{\sigma}_{eb'r}^2$  as

$$\tilde{\mu}_{eb'r} = \mu_{er} \left| \bigcup_{g \in \mathcal{G}_r} B_g \cup G_g^* \right| \quad \text{and} \quad \tilde{\sigma}_{eb'r}^2 = \sigma_{er}^2 \left| \bigcup_{g \in \mathcal{G}_r} B_g \cup G_g^* \right|.$$

An example of how merging and deleting operations update the group configuration in a region is shown in Fig. 4. The outcome of this procedure (summarized in Procedure 2) is a group configuration that better describes the elemental content in every region.

**Procedure 2.** Estimation of group configurations (see §4.2). Given regions  $\mathcal{R}$ , groups  $\mathcal{G}$ , elemental content  $c_r$ , and mean and variance of elemental content [e.g. from equations (5) and (6)];

**for all regions  $r \in \mathcal{R}$  do**

**repeat**

Set NumRegChanged = 0;

Evaluate null hypothesis  $\mathcal{L}(H_0|c_r)$ ;

Find  $\mathcal{L}(H'|c_r) := \max \mathcal{L}(H'|c_r)$  over  $H \in \Theta_0^C$ ;

**if**  $\mathcal{L}(H'|c_r) > \mathcal{L}(H_0|c_r)$  **then**

NumRegChanged = 1;

Update  $\mathcal{G}_r$  according to  $H'$ ;

**until** NumRegChanged = 0.

### 4.3. Optimization of group boundaries

The goal of our third procedure is to refine the area and location of each group so that the final shape and location best matches the elemental content for a particular type of cell to the given representative elemental content; see, for example, equations (5) and (6). We formulate this problem as an opti-

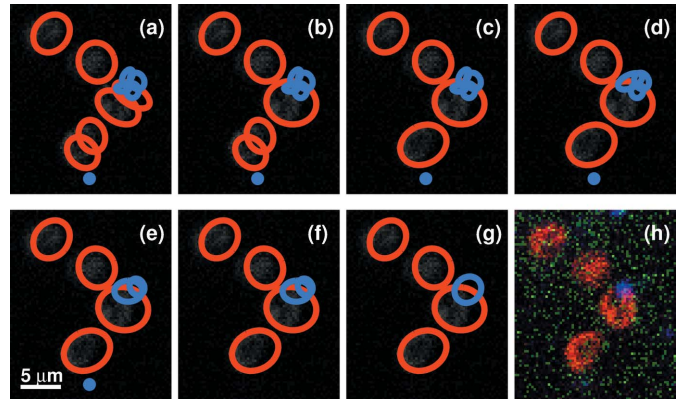


**Figure 4** Example of the progress of group merging and deleting operations. (a) Initial configuration; (b),(c) merging two red blood cell groups; (d),(e),(g) merging two yeast cell groups; (f) deleting a yeast cell group. The overlay of Mn (green), Fe (red) and Zn (blue) elemental maps (h) shows that this area contains four red blood cells and one yeast cell, which overlaps one of the red blood cells. The end configuration in (g) shows that the estimation procedure identifies this configuration correctly. Group boundaries are shown as ellipses for illustration only; all operations are based on taking the union of pixels.

mization problem and develop a gradient-sampling (Burke *et al.*, 2005) Gauss–Newton approach to solve it.

Previous approaches to this problem include region-growing methodologies by active contour (Chan & Vese, 2001), level sets (Caselles *et al.*, 1995; Malladi *et al.*, 1995) and snake (Kass *et al.*, 1988). Our technique also builds on the inside–outside model described by Amit (2002). Our approach differs from these techniques in that we focus on growing the inside region with multiple intensity channels taken into account simultaneously, and we use gradient sampling to approximate the steepest descent directions of overlapping groups.

Our partition of the image into regions allows us to treat the optimization over each region independently; in the remainder of this section we describe the optimization over a single region  $R_r$ .

The unknown variables in the optimization problem are the parameters that describe the shape and location of the boundary of each group. In our experiments we parameterized the boundaries using Daubechies wavelets (Daubechies, 1992) truncated at level  $d$ ,  $\{\psi_k(\tau) : k = 0, \dots, d\}$ , where  $\tau \in [0, 1]$ . The boundary of a group  $g \in \mathcal{G}_r$  is parameterized as  $\theta_g(\tau) = [\theta_{gx}(\tau), \theta_{gy}(\tau)]$  for  $x, y$  coordinates defined by wavelet coefficients  $u_{gk} = (u_{gkx}, u_{gky})$  as

$$\theta_g(\tau) = \sum_{k=0}^d u_{gk} \psi_k(\tau), \quad \text{for } \tau \in [0, 1]. \quad (14)$$

As a result, the unknowns in our optimization problems are the wavelet coefficients  $u = (u_{g0}, \dots, u_{gd})_{g \in \mathcal{G}_r}$ . In our experiments, these coefficients are initialized by fitting a minimum-area ellipse to each group generated in the previous step; see §4.2.

The objective function has two components: a proximal-point term that regularizes the objective and a data component that penalizes deviation of the group’s elemental content from typical elemental cell content. The proximal-point term is  $\|u - \bar{u}\|_\Lambda^2$ , where  $\bar{u}$  is the initial pasteurization (*e.g.* generated from a minimum-area ellipse). We use the squared scaled  $\ell_2$ -norm  $\|w\|_\Lambda^2 = w^T \Lambda w$ , where  $\Lambda = \text{dig}(\lambda_i)$  is a diagonal scaling matrix with  $1/\lambda_i$  as the variance of component  $i$  of  $u$ , which accounts for the different scales of wavelet coefficients from different levels  $k = 0, \dots, d$ .

The data objective penalizes violation of typical elemental content. For every cell type  $t \in \mathcal{T}$  and element  $e \in \mathcal{E}$ , we define bounds  $(L, U)$  that take the region background into account. In our experiments, we use bounds based on being within one standard deviation of the mean elemental content or

$$U_{ert} = \mu_{et} + \sigma_{et} + \mu_{er} \quad \text{and} \quad L_{ert} = \mu_{et} - \sigma_{et} + \mu_{er}.$$

Given these typical elemental bounds, we define the data objective for group  $g \in \mathcal{G}_r$  (of type  $t \in \mathcal{T}$ ) and element  $e \in \mathcal{E}$  as

$$h_e[c_e(u_g)] = \begin{cases} \frac{1}{2}[c_e(u_g) - U_{ert}]^2 & \text{if } c_e(u_g) \geq U_{ert}, \\ 0 & \text{if } L_{ert} < c_e(u_g) < U_{ert}, \\ \frac{1}{2}[c_e(u_g) - L_{ert}]^2 & \text{if } c_e(u_g) \leq L_{ert}, \end{cases} \quad (15)$$

where  $c_e(u_g) = c_{egt}$  is the assigned elemental content of the group  $G_g$  defined by the wavelet parameters  $u_g$ . The group’s area can be defined by an inverse wavelet transform. Summing the data objective over all elements, we define the region objective

$$J_r(u) = \sum_{g \in \mathcal{G}_r} \sum_{e \in \mathcal{E}} h_e[c_e(u_g)] + (\rho/2)\|u - \bar{u}\|_\Lambda^2, \quad (16)$$

where  $\rho$  is a predefined parameter regularizing between the data term and the proximal-point term. The function  $J_r(u)$  is in general nonsmooth (due to the pixellation effect), and we therefore employ gradient sampling to approximate the steepest descent direction. We accelerate the steepest descent step with a Gauss–Newton procedure that exploits the fact that we know the Hessian,  $\rho\Lambda$ , of the second term. We terminate our optimization if the data objective becomes zero or when we reach an iteration limit.

#### 4.4. Optimality test and local pixel refinement

In this section, we describe an optimality test for evaluating the local optimality of group boundaries obtained using the procedure in §4.3. We also propose a procedure that locally refines boundary pixels on groups that do not satisfy this optimality test.

For a given group  $G_g$ , we define its inside boundary  $N_g^-$  and outside boundary  $N_g^+$  as

$$N_g^- \equiv \{(x, y) \in G_g : \exists(x', y') \in B_g \text{ and } \|(x, y) - (x', y')\|_1 = 1\}, \\ N_g^+ \equiv \{(x, y) \in B_g : \exists(x', y') \in G_g \text{ and } \|(x, y) - (x', y')\|_1 = 1\}.$$

We also denote the updated objective  $J_r(u_g)$  as  $J_r(G_g)$  for the group of pixels  $G_g$ . We then define the following optimality test based on  $G_g, N_g^+$  and  $N_g^-$ :

**Optimality test 1.**  $G_g$  is said to have a locally optimal boundary if adding or deleting a single pixel does not improve  $J_r$ , that is, if  $J_r(G_g) \leq J_r(G_g \cup \{(x, y)\})$  for all  $(x, y) \in N_g^+$  and  $J_r(G_g) \leq J_r(G_g \setminus \{(x, y)\})$  for all  $(x, y) \in N_g^-$ .

If  $G_g$  does not satisfy this test, then we apply the local pixel refinement procedure (Procedure 3) to modify the boundary pixels of  $G_g$ . This procedure changes only one pixel at a time and repeats only *MaxIt* iterations. We employ this procedure for groups whose elemental contents are not within the range of  $[L_{ert}, U_{ert}]$  for at least one  $e \in \mathcal{E}$ , and we keep the *MaxIt* small (set to 5 in our experiments) so that the resulting  $G_g$  still maintains an approximately elliptic shape, as discussed in §4.1.1. This refinement procedure works for groups that are not overlapping with others because we have access to the exact  $J_r$  in the process of changing boundary pixels.

**Procedure 3.** Local pixel refinement (see §4.4).

Given pixel sets  $G_g$ ,  $N_g^-$  and  $N_g^+$ ;

**for**  $iter < MaxIt$  **do**

Let  $(x^+, y^+) = \underset{(x,y) \in N_g^+}{\operatorname{argmin}} J_r(G_g \cup \{(x, y)\})$

and set  $J_r^+ = J_r(G_g \cup \{(x^+, y^+)\})$ ;

Let  $(x^-, y^-) = \underset{(x,y) \in N_g^-}{\operatorname{argmin}} J_r(G_g \setminus \{(x, y)\})$

and set  $J_r^- = J_r(G_g \setminus \{(x^-, y^-)\})$ ;

**if**  $J_r(G_g) \leq \min(J_r^+, J_r^-)$  **then**

Locally optimal: **return**;

**else if**  $J_r^- < J_r^+$  **then**

Remove pixel  $(x^-, y^-)$  from  $G_g$ ;

**else**

Add pixel  $(x^+, y^+)$  to  $G_g$ ;

$iter = iter + 1$ .

**5. Results**

In this section, we present the results obtained from applying our approach to the test data set described in §3. Since the focus of using X-ray fluorescent microscopy is to study elemental contents of cells and we do not have manual annotations to compare with individual cells, our key metric of success is how well the elemental content distributions of the identified cell populations match the truncated Gaussian with their means represented by elemental content based on hand-drawn ROIs.

We evaluate the resulting cell populations based on the elemental distributions of each cell’s characteristic elements and multiple elements of well measurable quantities (*e.g.* yeast cells contain P, K, Zn, *etc.*). In addition, we are interested in how different the elemental contents from identified cell populations comparing with those from the hand-drawn ROIs, especially if these ROIs are informative enough for identifying the entire cell population. We expect contents of well measurable elements in given cell populations to be well above the estimated background derived from neighboring background pixels (§4.1.2) in their respective cell populations. Hence, as a byproduct, we also evaluate how well the background estimation works.

In Fig. 5, we show color-coded elemental content distributions (P, K, Mn, Fe, Zn) for the three cell types. These elemental distributions are the net contents after removal of estimated background. We also include an additional row showing the estimated background distributions. We observe the following:

(i) If a cell population contains well measurable amounts of specific elements, then the corresponding net contents (after removing background using neighbor background pixels) are well above zero. For example, the characteristic elements (Mn, Fe and Zn) are distinctly high in their respective cell populations; yeast cells also show high contents in P and K simultaneously. For those elements whose contents in cells are close to detection limits, their net content distributions can have both positive and negative values. This is because (a) the statistical nature of the collected signal can lead to negative

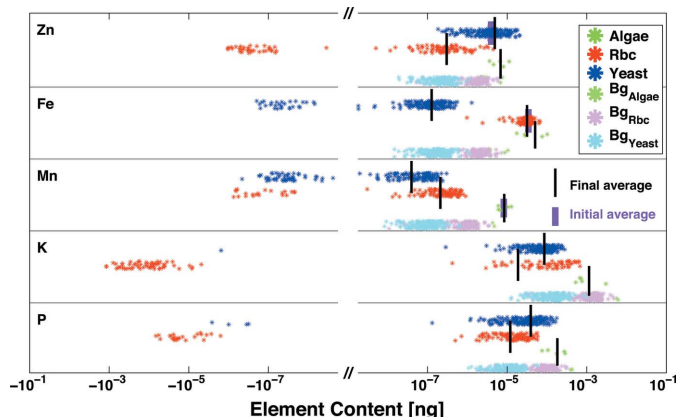


**Figure 5**

P, K, Mn, Fe, Zn content distributions of identified algae (green), yeast (blue) and red blood (red) cells. The light blue, pink and light green points indicate the estimated background (Bg) contents of the respective cell areas. The horizontal axis (log scale) shows net elemental content, and the points are distributed randomly within bounds in the vertical direction in order to provide separation. The magenta and black lines show, respectively, the initialized means from hand-drawn regions of interest, and the means of the actual cell populations in the characteristic elements. As expected, the cells tend to have high elemental content in their characteristic elements: red blood cells have high Fe content, and yeast cells contain significant amounts of P and Zn. Some elements can show negative content for some cells (the K channel in red blood cells, for example); this is because of the need to subtract substrate and background signals from the raw elemental content to calculate the actual elemental content for a given cell. In case the signal is close to zero, the statistical nature of the collected signal can lead to negative values when two nearly equal signals are subtracted.

numbers when two nearly equal signals are subtracted; (b) some of these elements contain ‘halo’ regions: if the identified cells do not contain large quantities of these elements and they are inside of these regions (*e.g.* K content in red blood cells), we can obtain negative net contents.

(ii) The distances between the magenta and black lines show how much the initial guesses from a few hand-drawn ROIs differ from the means of the cell populations determined by our method. The mean contents from the identified cell populations (>100 cells) are within 20% ranges compared with the mean contents from hand-drawn ROIs, which include no more than ten cells. This indicates that the cell populations in our dataset have consistent elemental contents, especially in their respective characteristic elements.

(iii) We observe that the iron content values we obtained are in a reasonably good agreement with literature values. For example, for red blood cells we measure a mean Fe content of about 50 fg per cell (see Fig. 5), which compares with 60–80 fg per cell as reported by Jones (1975) and Hewitt *et al.* (1989). The difference may be due to possible elemental redistribution due to the sample preparation procedure, the limited statistics we employed, an underestimate of cell size, or an overestimate of background contribution.

To summarize, we observe that all identified cells have significant contents that match their respective biological expectations. These elemental contents are different from the mean contents of the hand-drawn ROIs by about 20%. Furthermore, our background estimation works well for

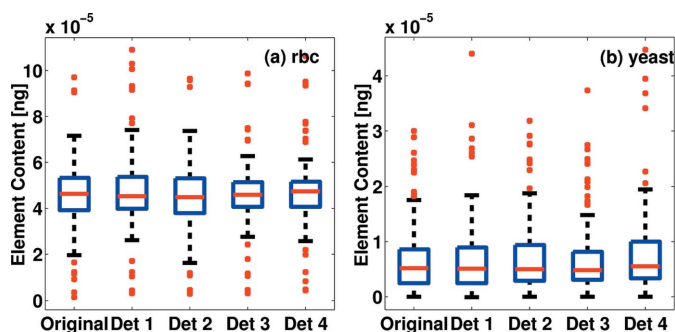
elements with well measurable amounts in given cell populations.

### 6. Discussion and validation

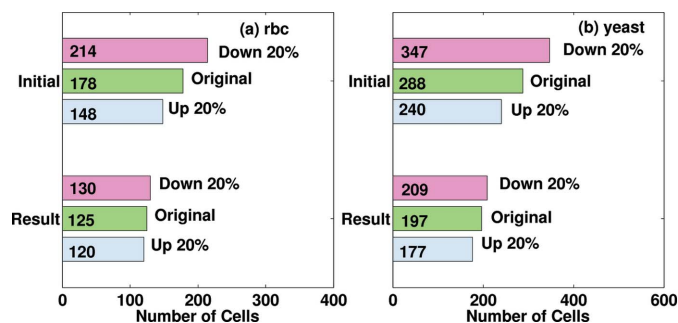
The cell identification results we report in §5 use the sum of the four detector measurements, where each detector segment records the fluorescence signal from a slightly different viewing angle. This can lead to slight variations in calculated elemental concentration because of variations in scattering background and absorption of fluorescence signal along the viewing path. To validate that the identified cell areas do contain cells, we applied this approach to each elemental concentration map separately and compared the elemental distributions of all resulting cell populations. Our assumption is that if an area contains actual cells, all four detectors will measure significant elemental signals from it. In this case, if our approach identifies similar cells from all four individual measurements and the sum of them, this identification agreement provides evidence that our approach finds cells correctly.

Fig. 6 shows the elemental content from the resulting red blood and yeast cells (there are only five algae cells). These scatterplots show that the Fe distributions of resulting red blood cells and the Zn distributions of resulting yeast cells are similar. An ANOVA test (Rice, 1995) determines that none of the five cell populations has statistically significant differences in elemental distribution. Hence we conclude that this identification approach using different measurements of the same sample recognizes similar elemental distributions of each resulting cell population.

We also examined the dependence on the initial determination of foreground and background regions. In the preprocessing step, we divide pixels into foreground and background components based on the thresholding pixel intensity in the their characteristic elemental maps. We eval-



**Figure 6** (a) Boxplot of Fe distributions from red blood cells obtained using the separate detector segments as well as their sum. (b) Boxplot of Zn distributions from yeast cells obtained using separate detector segments as well as their sum. This figure demonstrates that elemental contents obtained by separate analysis from the different detector segments are similar, adding confidence in the robustness of our results. The central mark is the median, the edges of the boxes denote the 25th and 75th percentiles, the whiskers extend to the most extreme data points not considered outliers, and the outliers are plotted individually.



**Figure 7** Test of the total number of red blood cells (a) and yeast cells (b) identified as the initial choice for elemental thresholding is changed over a 20% range. Of course the initial threshold choice has a strong direct effect on the initial number of putative cells found by the algorithm. The effect of this initial parameter choice is greatly reduced at the end of our analysis sequence, as is shown by the comparative robustness of the resulting cell number.

uate the robustness of our approach by varying the threshold  $\pm 20\%$ . This thresholding variation changes the initial group configurations.

We would like to evaluate whether we can obtain similar cell identification results using initial group configurations from these three different thresholds. If we obtain similar cell identification result, we believe that our approach is robust with respect to threshold variation in the  $\pm 20\%$  range.

The up/down thresholding changes the number of initial groups ('Initial' in Fig. 7) by 15–20%, whereas the numbers of cells among all resulting cell populations ('Result' in Fig. 7) differ only by 5–8%. For example, the preprocessing procedure obtains 288 initial yeast cell groups using the original threshold, and there are 197 yeast cells in the resulting cell population; using downthresholding, the preprocessing obtains 347 initial (a 20% difference) and 209 final (a 6% difference) yeast cell groups. These results illustrate that our

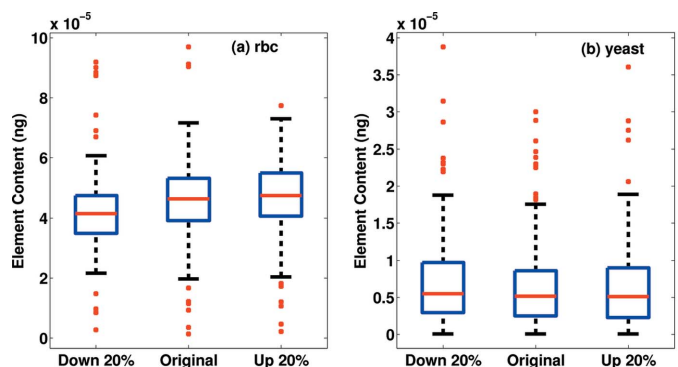


**Figure 8** Boxplots showing (a) Fe distributions in red blood cell populations and (b) Zn distributions in yeast cell populations resulting from three different initial elemental thresholding choices. The similarity of results shows that the results obtained are robust against changes in initial parameters. The central mark is the median, the edges of the boxes denote the 25th and 75th percentiles, the whiskers extend to the most extreme data points not considered outliers, and the outliers are plotted individually.

final cell populations are relatively insensitive to the different thresholding; the final results change only by  $\pm 8\%$ .

We also compare the elemental contents of cell populations resulting from the three different initial threshold choices. The scatterplots in Fig. 8 show that both the Zn distributions of the resulting yeast cell populations and Fe distributions of the resulting red blood cells are insensitive to the different thresholding. Furthermore, we found no significant difference in the means of all three Zn (and Fe) distributions using a one-way ANOVA test.

These results show that our approach is able to estimate elemental content of cell populations very well, with final results being insensitive to modest changes in initial input parameters.

## 7. Conclusion and future work

We describe here an approach for identifying cells of complex configurations (including heavily overlapping cells) in multi-dimensional XFM datasets. Without explicit expert knowledge and training using manual annotation, we demonstrate that this approach can identify and differentiate multiple cell types based on their respective trace elemental content. The generalized likelihood ratio test is robust in determining cell configurations using initial putative groups generated by using various elemental content thresholds. Furthermore, our approach shows consistent performance in processing regions with overlapping structures, where it is difficult or impossible to obtain reliable cell identification manually, and easily deals with the volume and complexity of current microscopy data. On a large dataset such as the test dataset shown here, our algorithm takes about an hour of total processing time on a personal laptop, with segmentation taking about 5 min, estimation of regions about 45 min, and boundary delineation and pixel refinement another 10 min. The computing time scales linearly with the number of regions, and exponentially with the number of cells in each region. (This is ten times faster compared with the *MAPS* routine in obtaining fitted data. Also, our segmentation runs in seconds, which is comparable with running the ‘analyze particle’ routine in *ImageJ*.)

As we discussed in §1, our method extends other unsupervised cell identification methods in that we incorporate into the likelihood test as many independent elements simultaneously as needed, and model overlapping cells to determine their respective elemental content. For example, the common cell counting routine ‘analyze particles’ in *ImageJ* (Abramoff *et al.*, 2004) only processes one independent intensity channel at a time, whereas we use all nine elemental maps simultaneously to determine cells. In addition, its approach to cell shape estimation, namely the generation of cell segments based on the thresholding and subsequent clustering based on pixel positions, is similar to our preprocessing segmentation. Our approach extends this by effectively incorporating cell properties such as total elemental content and cell morphology to identify whole cells (*i.e.* noncontiguous nearby pixels are not mistakenly identified as multiple cells).

Extensions that we plan to integrate into this methodology include the modeling of cell size and shape, adapting the covariance matrix according to the cell size, and in particular making this approach iterative so that the result from the pixel refinement is fed back to the estimation of group configurations to further improve the identification. From the computational perspective, our next step will be to exploit the mutual independence of regions to parallelize our algorithm, as well as to optimize the code for processing speed.

We are aware that this test dataset contains cells with distinct elemental contents. This condition simplifies the initialization part of our cell identification. A natural extension would be to expand the scope of our algorithm in order to study more complicated cases, including cells with arbitrary shapes, sizes and heterogeneous (*i.e.* non-Gaussian) elemental content distributions, and to analyze full XFM spectra. In addition, we are interested in developing metrics to measure quantitatively the performance of this type of unsupervised approach, possibly aided by image registration with other types of images (*e.g.* from optical microscopy).

This work was supported by the US Department of Energy, Office of Science, Advanced Scientific Computing Research, and Basic Energy Sciences program (DE-AC02-06CH11357). We thank Qiaoling Jin and Sophie-Charlotte Gleber for helpful suggestions. We are grateful for comments from the referees, which have helped the presentation.

## References

- Abramoff, M. D., Magelhaes, P. J. & Ram, S. J. (2004). *Biophoton. Intl.* **11**, 36–42.
- Amit, Y. (2002). *2D Object Detection and Recognition: Models, Algorithms and Networks*. Cambridge: MIT Press.
- Arteta, C., Lempitsky, V., Noble, J. A. & Zisserman, A. (2012). *Proceedings of the 15th International Conference on Medical Image Computing and Computer-Assisted Intervention (MICCAI12)*, pp. 348–356. Berlin: Springer-Verlag.
- Aydin, Z., Murray, J., Waterston, R. & Noble, W. (2010). *BMC Bioinformatics*, **11**, 1–13.
- Bergeest, J.-P. & Rohr, K. (2011). *Lect. Notes Comput. Sci.* **6891**, 645–652.
- Bergeest, J.-P. & Rohr, K. (2012). *Med. Image Anal.* **16**, 1436–1444.
- Burke, J. V., Lewis, A. S. & Overton, M. L. (2005). *SIAM J. Optim.* **15**, 751–779.
- Caselles, V., Kimmel, R. & Sapiro, G. (1995). *Intl J. Comput. Vis.* **22**, 61–79.
- Chan, T. & Vese, L. (2001). *IEEE Trans. Image Process.* **10**, 266–277.
- Cortés, L. & Amit, Y. (2008). *IEEE Trans. Pattern Anal. Mach. Intell.* **30**, 1998–2010.
- Daubechies, I. (1992). *Ten Lectures on Wavelets, CBMS-NSF Regional Conference Series in Applied Mathematics*. Philadelphia: SIAM.
- Dhillon, I., Guan, Y. & Kulis, B. (2007). *IEEE Trans. Pattern Anal. Mach. Intell.* **29**, 1944–1957.
- Dismukes, G. C. (1986). *Photochem. Photobiol.* **43**, 99–115.
- Good, N. E., Winget, G. D., Winter, W., Connolly, T. N., Izawa, S. & Singh, R. M. (1966). *Biochemistry*, **5**, 467–477.
- Gorman, D. S. & Levine, R. P. (1965). *Proc. Natl Acad. Sci. USA*, **54**, 1665–1669.
- Hawkins, W. W., Speck, E. & Leonard, V. G. (1954). *Blood*, **9**, 999–1007.

- Hewitt, C., Innes, D., Savory, J. & Wills, M. (1989). *Clin. Chem.* **35**, 1777–1779.
- Jones, R. (1975). *Lab. Anim.* **9**, 143–147.
- Kass, M., Witkin, A. & Terzopoulos, D. (1988). *Intl J. Comput. Vis.* **1**, 321–331.
- Kasson, P. M., Huppa, J. B., Davis, M. M. & Brunger, A. T. (2005). *Bioinformatics*, **21**, 3778–3786.
- Kirz, J. (1980). *Ultrasoft X-ray Microscopy: Its Application to Biological and Physical Sciences*, edited by D. F. Parsons, *Annals of the New York Academy of Sciences*, pp. 273–287. New York, USA.
- Lerotic, M., Jacobsen, C., Gillow, J., Francis, A., Wirick, S., Vogt, S. & Maser, J. (2005). *J. Electron Spectrosc. Relat. Phenom.* **144–147**, 1137–1143.
- Lerotic, M., Jacobsen, C., Schäfer, T. & Vogt, S. (2004). *Ultramicroscopy*, **100**, 35–57.
- Lin, G., Adiga, U., Olson, K., Guzowski, J. F., Barnes, C. A. & Roysam, B. (2003). *Cytometry A*, **56A**, 23–36.
- Ljosa, V. & Carpenter, A. E. (2009). *PLoS Comput. Biol.* **5**, e1000603.
- Lundblad, V. & Struhl, K. (2001). *Current Protocols in Molecular Biology*, pp. 13.0.1–13.0.4. Hoboken: John Wiley.
- McCullough, D. P., Gudla, P. R., Harris, B. S., Collins, J. A., Meaburn, K. J., Nakaya, M. A., Yamaguchi, T. P., Misteli, T. & Lockett, S. J. (2008). *IEEE Trans. Med. Imaging*, **27**, 723–734.
- Malladi, R., Sethian, J. & Vemuri, B. (1995). *IEEE Trans. Pattern Anal. Mach. Intell.* **17**, 158–175.
- Marvin, R., Wolford, J., Kidd, M., Murphy, S., Ward, J., Que, E., Mayer, M., Penner-Hahn, J., Haldar, K. & O' Halloran, T. (2012). *Chem. Biol.* **19**, 731–741.
- Paunesku, T., Vogt, S., Maser, J., Lai, B. & Woloschak, G. (2006). *J. Cell. Biochem.* **99**, 1489–1502.
- Plaza, A., Martinez, P., Perez, R. & Plaza, J. (2004). *Pattern Recognit.* **37**, 1097–1116.
- Rice, J. A. (1995). *Mathematical Statistics and Data Analysis*, 2nd ed. Belmont: Duxbury Press.
- Russell, C., Metaxas, D., Restif, C. & Torr, P. (2007). *2007 IEEE International Conference on Computer Vision*, pp. 2362–2369.
- Ryan, C., van Achterbergh, E., Yeats, C., Win, T. T. & Cripps, G. (2002). *Nucl. Instrum. Methods Phys. Res. B*, **189**, 400–407.
- Solé, V., Papillon, E., Cotte, M., Walter, P. & Susini, J. (2007). *Spectrochim. Acta B*, **62**, 63–68.
- Swedlow, J. R., Goldberg, I. G. & Eliceiri, K. W. (2009). *Annu. Rev. Biophys.* **38**, 327–346.
- Tan, M., Braga, R. A., Fink, R. W. & Rao, P. V. (1982). *Phys. Scr.* **25**, 536.
- Tao, C. Y., Hoyt, J. & Feng, Y. (2007). *J. Biomol. Screen.* **12**, 490–496.
- Vogt, S. (2003). *J. Phys. IV*, **104**, 635–638.
- Wang, M., Zhou, X., Li, F., Huckins, J., King, R. W. & Wong, S. T. C. (2007). *Bioinformatics*, **24**, 94–101.
- Wasserman, L. (2003). *All of Statistics: A Concise Course in Statistical Inference*. Berlin: Springer.
- Wolz, R., Heckemann, R. A., Aljabar, P., Hajnal, J. V., Hammers, A., Lötjönen, J. & Rueckert, D. (2010). *NeuroImage*, **52**, 109–118.
- Wu, B. & Nevatia, R. (2009). *Intl J. Comput. Vis.* **82**, 185–204.
- Yin, Z., Bise, R., Chen, M. & Kanade, T. (2010). *IEEE International Symposium on Biomedical Imaging (ISBI)*, pp. 125–128.